Structure and Electronic Properties of Solid Acids Based on Tungsten Oxide Nanostructures

David G. Barton,[†] Max Shtein,[†] Ryan D. Wilson,[†] Stuart L. Soled,[‡] and Enrique Iglesia*[,†]

Department of Chemical Engineering, University of California at Berkeley, Berkeley, California 94720, and Corporate Research Laboratory, Exxon Research and Engineering, Route 22 East, Annandale, New Jersey 08801

Received: August 27, 1998; In Final Form: November 16, 1998

UV−visible diffuse reflectance spectroscopy was used to probe the electronic structure and domain size of tungsten oxide species in crystalline isopolytungstates, monoclinic WO_3, and dispersed WO_x species on ZrO_2 surfaces. UV−visible absorption edge analysis, CO_2 chemisorption, and Raman spectroscopic results show that three distinct regions of WO_x coverage on ZrO_2 supports appear with increasing WO_x surface density: submonolayer region (0−4 W nm^{-2}), polytungstate growth region (4−8 W nm^{-2}), and polytungstate/crystalline WO_3 coexistence region (>8 W nm^{-2}). The structure and catalytic activity of WO_x species on ZrO_2 is controlled only by WO_x surface density (W nm^{-2}), irrespective of the WO_x concentration, oxidation temperature, and ZrO_2 surface area used to obtain a particular density. The submonolayer region is characterized by distorted octahedral WO_x species that are well dispersed on the ZrO_2 surface. These species show a constant absorption edge energy, they are difficult to reduce, and contain few acid sites where *o*-xylene isomerization can occur at 523 K. At intermediate WO_x surface densities, the absorption edge energy decreases, WO_x domain size increases, WO_x species become easier to reduce, and *o*-xylene isomerization turnover rates (per W atom) increase with increasing WO_x surface density. At high WO_x surface densities, a polytungstate monolayer coexists with monoclinic WO_3 crystallites. The growth of monoclinic WO_3 crystallites results in lower *o*-xylene isomerization turnover rates because WO_x species become inaccessible to reactants. In the presence of H_2 at typical catalytic reaction temperatures (∼523 K), strong acid sites form on WO_x−ZrO_2 catalysts with polytungstate domains by a slight reduction of the cluster and delocalization of an electron from an H atom resulting in $H^{+\delta}$ (Brønsted acid site).

1. Introduction

Strong solid acids based on supported transition-metal oxides are potential replacements for liquid acids and halide-containing solids.[1,2] Acid site strengths and densities similar to those in sulfuric acid, halides, or oxyhalides remain elusive. Brønsted acid sites form on oxide-based solid acids when protons balance net negative charges introduced by substituting cations with a lower valence charge[3] or by partial reduction of neutral oxide clusters.[4] Sulfuric acid impregnated on zirconia supports has been extensively studied as a strong solid acid;[5,6] their poor stability and their tendency to form volatile sulfur compounds during catalysis and regeneration limit their applicability in isomerization and alkylation processes.[7]

Tungsten oxide species dispersed on zirconia supports (WO_x−ZrO_2) comprise another interesting class of solid acids. Hino and Arata first suggested that strong acid sites form on these materials when zirconia oxyhydroxide ($ZrO_x(OH)_{4-2x}$) is impregnated with solutions containing tungstate anions and then oxidized at high temperatures (873−1173 K).[8] They reported low-temperature catalytic activity for *n*-pentane and *n*-hexane isomerization, but cracking selectivities were very high (>50%), even at low conversions.[9] The addition of a small amount of platinum (<1 wt % Pt) to preoxidized WO_x−ZrO_2 samples leads to active, stable, and selective catalysts for *n*-alkane isomerization reactions when hydrogen is present.[4,10−13] On Pt/WO_x−ZrO_2 we have shown that efficient hydrogen transfer steps prevent extensive cracking of adsorbed carbocations by limiting their surface lifetimes.[4] Several recent patents describe the synthesis and catalytic activity of WO_x−ZrO_2 and Pt/WO_x−ZrO_2 for several hydrocarbon reactions (cyclohexane ring-opening and isomerization, benzene hydrogenation, alkene oligomerization, aromatic alkylation with alkenes or methanol, aromatic trans-alkylation, and heteroatom removal).[14]

High turnover rates for acid-catalyzed isomerization on WO_x−ZrO_2 catalysts require the presence of WO_x domains of intermediate size on ZrO_2 surfaces.[4] Maximum *o*-xylene isomerization turnover rates occur at WO_x surface densities (8−10 W nm^{-2})[15] that exceed the theoretical monolayer capacity of ZrO_2 (7 W nm^{-2}).[16] *o*-Xylene isomerization turnover rates depend only on WO_x surface density and not independently on WO_x concentration, oxidation temperature, or ZrO_2 surface area. The presence of H_2 during *o*-xylene isomerization increases turnover rates and prevents rapid deactivation.[15] X-ray absorption studies have shown that W centers reside in similar distorted octahedral environments for a wide range of WO_x surface densities (3−15 W nm^{-2}).[4] WO_x domains of intermediate size appear to provide a compromise between reducibility and accessibility of WO_x centers. These WO_x domains delocalize a net negative charge caused by the slight reduction of W^{6+} centers leading to the in situ formation of Brønsted acid centers $(WO_3)_n$-$\{W^{6-\delta}-O_3\}\{H^{+\delta}\}$ in reactant environments containing H_2 or hydrocarbons.[17]

* Author to whom correspondence should be addressed. Fax: (510) 642-4778. E-mail: iglesia@cchem.berkeley.edu.
[†] University of California at Berkeley.
[‡] Exxon Research and Engineering.

10.1021/jp983555d CCC: $18.00
Published on Web 01/09/1999

UV−visible diffuse reflectance spectroscopy is a useful spectroscopic technique that probes the electronic structure and domain size of transition-metal oxides. The position of the absorption edge is sensitive to the bonding between metal oxide polyhedra,[18] and it has been used to characterize the average particle size of nano-crystalline insulators and semiconductors.[19] In our study, UV−visible absorption edge energies of WO_x species on ZrO_2 supports are compared with the edge energies of several crystalline standards with known WO_x coordination symmetry and domain size in order to determine how acid-catalyzed reaction rates depend on bonding between WO_x species and WO_x domain size. In addition, color changes associated with the reduction of these WO_x domains in H_2 at *o*-xylene reaction temperatures (523 K) are measured by the appearance of absorption bands at energies below the absorption edge. The rate of reduction of these neutral WO_x domains may be related to the ability of these materials to form Brønsted acid sites under reaction conditions.

Raman spectroscopy is a valuable tool for the characterization of dispersed metal oxides. It detects vibrational modes of surface and bulk structures, which can be related to molecular structures by comparison with standard compound spectra or with theoretical calculations. The accuracy, reliability, and interpretation of the Raman spectra of metal oxide catalysts have been discussed recently.[20] Supported tungsten oxide catalysts have been widely studied, with emphasis on samples with low WO_x surface densities on γ-Al_2O_3 supports.[21] Some recent studies of WO_x−ZrO_2 samples have detected polytungstate and crystalline WO_3 species at relative concentrations that depend on WO_x concentration and oxidation temperature.[22−24] In this study, Raman spectroscopy is used to determine how the intensity of bands corresponding to the internal W−O stretch in bulk WO_3 crystallites and the terminal W═O stretch are related to the dispersion of WO_x species for dehydrated WO_x−ZrO_2 samples with a wide range of WO_x concentrations (3−26 wt % WO_3) and oxidation temperatures (933−1283 K).

2. Experimental Section

2.1 Synthesis. $ZrO_x(OH)_{4-2x}$ supports (295 m^2 g^{-1}) were prepared by the hydrolysis of 0.5 M $ZrOCl_2$ (Aldrich Chemicals, >98%) aqueous solutions fed at 500 cm^3 h^{-1} into a well-stirred vessel with a pH of 10 held constant by the controlled addition of NH_4OH (14 N). The precipitate was dried at 423 K overnight after residual Cl^- ions were removed (<10 ppm) by thorough washing. The dry $ZrO_x(OH)_{4-2x}$ solids were impregnated to the point of incipient wetness with ammonium metatungstate ($(NH_4)_6H_2W_{12}O_{40}$, Strem Chemical, 99.9+%) aqueous solutions. These samples were placed in shallow quartz boats (5 g each), heated at 0.167 K s^{-1} to the final oxidation temperature (773−1283 K), and held isothermal for 3 h in dry air flowing through a 25 mm quartz tube (4 cm^3 s^{-1}). Tungsten oxide loadings are reported as a percent by weight of WO_3 (0−26 wt % WO_3) in the oxidized (dehydrated) samples. Several samples were analyzed by atomic absorption to confirm the accuracy of these nominal WO_x loadings (± 0.3 wt % WO_3) and to show that WO_x does not sublime even at the highest oxidation temperatures of our study.

2.2 UV−Visible Diffuse Reflectance Spectroscopy. Ultraviolet−visible (UV−vis) diffuse reflectance spectra of WO_x−ZrO_2 samples and standard WO_x compounds were obtained using a Varian (Cary 4) spectrophotometer with a Harrick-Scientific Praying-Mantis diffuse reflectance accessory and in situ cell (DRA-2CR). Samples were lightly ground using an agate mortar and pestle to form agglomerates smaller than 0.1 mm and dehydrated in the reflectance accessory at 723 K for 2 h in flowing dry air (Matheson, Ultra Zero Grade, 2.0 cm^3 s^{-1}) purified with a 13X molecular sieve in order to remove residual water and hydrocarbons. The Kubelka−Munk function ($F(R_\infty)$, eq 2) for infinitely thick samples was used to convert reflectance measurements (R_{sample}) into equivalent absorption spectra[25] using the reflectance of MgO as a reference (R_{MgO}).

$$R_\infty = \frac{R_{sample}}{R_{MgO}} \tag{1}$$

$$F(R_\infty) = \frac{(1 - R_\infty)^2}{2R_\infty} = \frac{\alpha(\text{absorption coefficient})}{S(\text{scattering coefficient})} \tag{2}$$

2.3 Chemisorption Studies. Chemisorption data were collected using a Quantachrome 1C Autosorb apparatus. Samples were heated in He at 0.083 K s^{-1} to 673 K and held for 4 h in order to remove adsorbed H_2O and CO_2 before CO_2 adsorption measurements. After cooling to 313 K, samples were evacuated and a CO_2 adsorption isotherm was obtained between 2.7 and 53 kPa. The low-pressure linear part of the isotherm was extrapolated to zero pressure to calculate chemisorption uptakes. Samples for H_2 chemisorption were dried at 723 K in air and reduced in H_2 at 523 K for 1 h. After evacuation, H_2 adsorption isotherms were obtained between 2.7 and 53 kPa H_2 at 523 K. Physical surface areas were obtained by N_2 physisorption at 77 K (after dehydration in N_2 for 2 h at 473 K) using a Quantasorb surface area analyzer (Quantachrome Corporation) and standard multi-point BET methods.

2.4 Raman Spectroscopy. Raman spectra were obtained using a HoloLab 5000 Research Raman Spectrometer (Kaiser Optical Systems, Inc.) equipped with a 532 nm diode-pumped solid-state laser (Coherent Laser Group) and a thermoelectrically cooled CCD detector (Princeton Instruments, Inc.). WO_x−ZrO_2 samples were pressed into 1.0 cm diameter wafers and placed within a controlled atmosphere quartz cell containing Heraeus Amersil Suprasil 311 quartz optical windows. Samples were dehydrated in situ by heating to 673 K in flowing air (Zero Grade, 1 cm^3 s^{-1}) for 1 h and then cooled to 373 K to measure Raman spectra. Spectra were normalized by the applied laser power (laser exposure time). Mixtures of Lorentzian and Gaussian basis functions were chosen to fit Raman spectra using nonlinear least-squares methods.

3. Results/Discussion

3.1 Analysis of UV−Visible Absorption Edge Energy. The optical absorption edge energies of crystalline and amorphous WO_x species were obtained from diffuse reflectance UV−vis absorption spectra. The optical absorption edge energy is defined as the minimum photon energy required to excite an electron from the highest occupied molecular orbital (HOMO, at the top of the valence band in semiconductor domains) to the lowest unoccupied molecular orbital (LUMO, at the bottom of the conduction band). There are two basic types of electronic transitions, direct and indirect.[26] Direct transitions require only that photons excite electrons, while indirect transitions also require concerted vibrations and energy from the crystal lattice (phonons). The energy dependence of the absorption coefficient (α) for semiconductors in the region near the absorption edge is given by

$$\alpha \propto \frac{(h\nu - E_o)^\eta}{h\nu} \tag{3}$$

where $h\nu$ is the energy of the incident photon and E_o is the optical absorption edge energy; the exponent η depends on the type of optical transition caused by photon absorption.[26] In crystalline semiconductors, where crystal momentum is conserved and electron transitions obey well-defined selection rules, η is 1/2, 3/2, 2, and 3 when the transitions are direct-allowed, direct-forbidden, indirect-allowed, and indirect-forbidden, respectively. In general, transitions that are forbidden by symmetry selection rules have a lower probability of occurring [$P_i \propto (h\nu - E_o)$] and transitions that require phonons have an additional $(h\nu - E_o)^{3/2}$ factor that arises from the dependence of the absorption coefficient on phonon energy. In amorphous, homogeneous semiconductors, the value of η is 2 irrespective of the type of transition found in crystalline materials of the same composition.[27] The momentum vector is not conserved in amorphous materials; therefore, an integration has to be performed over the density of states, resulting in an energy dependence similar to that for indirect transitions.

With an appropriate choice of η, a plot of $(\alpha h\nu)^{1/\eta}$ vs $h\nu$ is linear near the edge and the intercept of the line on the abscissa (at $(\alpha h\nu)^{1/\eta} = 0$) gives the optical absorption edge energy E_o. Previous studies have shown that the fundamental absorption edge of WO_3 crystallites is caused by indirect electron transitions[28] and that a plot of $(\alpha h\nu)^{1/2}$ vs $h\nu$ is linear near the edge for amorphous WO_3 films.[29] We find a similar linear dependence for small WO_x domains, for which band theory does not strictly apply. A large density of available 5d states and static disorder in W−O bond lengths and angles leads to a broad distribution of states that can be analyzed using methods applicable to bands of energy levels. Therefore, a value of $\eta = 2$ was used in this study in order to define the absorption edge for WO_x−ZrO_2 samples containing crystalline WO_3 or amorphous WO_x species in isolated or polytungstate domains.

In the diffuse reflectance experiments, UV−vis reflectance data cannot be used directly to measure absorption coefficients (α) because of scattering contributions to the reflectance spectra. Scattering coefficients, however, depend weakly on energy and $F(R_\infty)$ can be assumed to be proportional to the absorption coefficient within the narrow range of energy containing the absorption edge features. Then, a plot of $(F(R_\infty)\bullet h\nu)^{1/\eta}$ vs $h\nu$ can be used to determine the absorption edge energy. An excellent fit was obtained using this method ($\eta = 2$) for amorphous WO_x domains on ZrO_2 and for a crystalline monoclinic WO_3 sample (Figure 1), which confirms that this method gives a precise value of the absorption edge energy (±0.03 eV). Most absorption spectra in this study, including those of molecular WO_x clusters, are also described accurately in this manner as determined by the linearity of the plot when $\eta = 2$. WO_x−ZrO_2 samples containing two or more distinct WO_x structures, however, require deconvolution to separate the multiple absorption edges. The nonlinear region found at energies lower than E_o is known as the Urbach tail;[30] it is related to low-frequency acoustic modes that lead to fluctuations in the band gap. It is often represented by an empirical relation valid for $h\nu < E_o$:

$$\alpha \propto \exp[\rho(h\nu - E_o)/kT] \qquad (4)$$

where σ is a constant.

It is interesting to note that the other crystalline d^0 transition metal oxides (MoO_3, V_2O_5, and TiO_2) also show an indirect absorption edge and can be analyzed by the method outlined above (with $\eta = 2$).[31] Several studies, however, have described UV−vis spectra using the formalism for direct-allowed transitions ($\eta = {}^1/_2$)[18,32] or the position of the first absorption maximum.[33,34] Methods based on direct transitions or peak position emphasize the region of high optical absorption near the edge, where the Kubelka−Munk function becomes nonlinear in absorber concentration and underlying assumptions become inaccurate.[35]

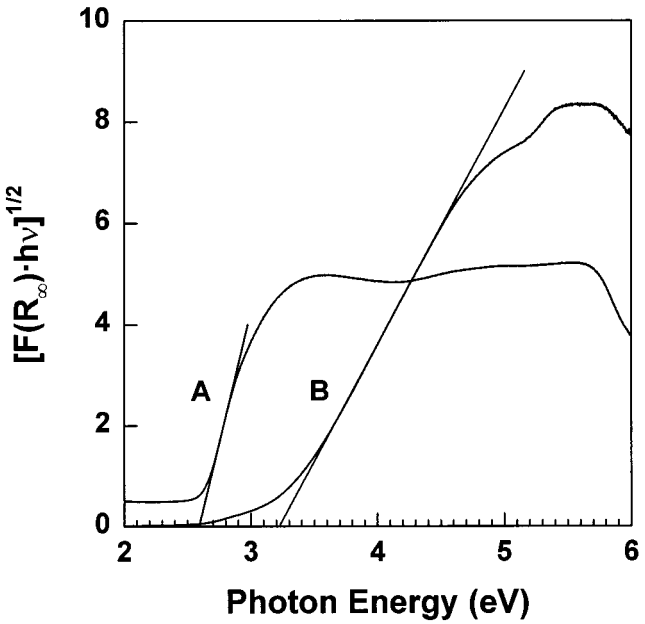

Figure 1. Absorption edge energies are determined by the intercept of a linear fit to the absorption edge. (A) Monoclinic WO_3 ($E_o = 2.59$ eV) and (B) 15% WO_x−ZrO_2, 1073 K oxidation ($E_o = 3.22$ eV) are shown for example.

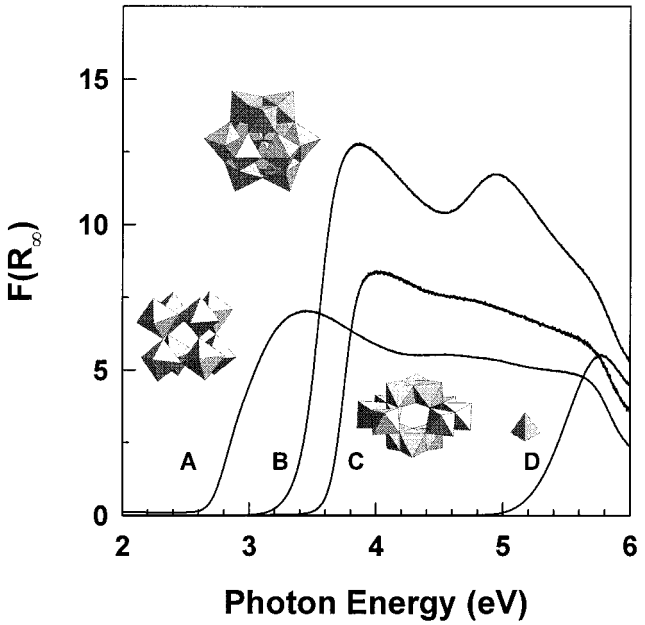

Figure 2. Diffuse reflectance UV−vis absorption spectra of crystalline tungsten oxide reference compounds: (A) monoclinic WO_3; (B) metatungstate, $(NH_4)_6H_2W_{12}O_{40}$; (C) paratungstate, $(NH_4)_{10}H_2W_{12}O_{42}$; and (D) Na_2WO_4.

3.2 UV−Visible Absorption Spectra of Tungsten Oxide Standards. UV−vis absorption spectra were measured for various crystalline WO_x standard compounds of known composition and structure. These samples cover a wide range of WO_x domain size, coordination symmetry, and absorption edge energy (Figure 2). Dehydrated $Na_2WO_4\cdot H_2O$ (Aldrich Chemicals, 99.995%) consists of molecular (isolated) four-coordinate W^{6+} centers tetrahedrally coordinated to oxygens[36] and gave the highest absorption edge energy value (4.89 eV) among the

samples examined. Six-coordinate W^{6+} in monoclinic WO_3 (Aldrich Chemicals, 99.995%), which contains WO_x species in an extended three-dimensional crystalline network of distorted octahedra bonded to six neighboring octahedra (distorted ReO_3 structure[37]), gave the lowest absorption edge energies (2.59 eV). WO_x domains of intermediate size, such as those found in isopolytungstate clusters containing octahedra bonded through corners and edges, showed intermediate values of the absorption edge energies. For example, absorption edge energies for W_{12} clusters in ammonium metatungstate [$(NH_4)_6H_2W_{12}O_{40}$, Strem Chemicals, 99.9+%] and ammonium paratungstate [$(NH_4)_{10}H_2W_{12}O_{42}$, K&K Laboratories 99.9%] were 3.23 and 3.54 eV, respectively.

The absorption edge energy for these crystalline WO_x standards is strongly influenced by the number of WO_x polyhedra neighbors bonded through W−O−W bonds and by the number of bonds between each polyhedra. Quasi-infinite WO_x domains in monoclinic WO_3 contain WO_6 octahedra with six WO_6 neighbors and have an edge energy that is 2.3 eV lower than that found for isolated WO_x species. The smaller difference in the absorption edge energies between the two polytungstate clusters, both of which contain WO_6 octahedra with four WO_6 neighbors, reflects differences in bonding between the WO_6 octahedra. Metatungstate contains a larger fraction of edge-sharing octahedra relative to corner-sharing octahedra and therefore has greater molecular orbital overlap between octahedra and a narrower HOMO−LUMO gap because of the more extensive "communication" of electrons between octahedra.

Weber[18] reported an apparent linear correlation between the number of nearest MoO_x neighbors in crystalline MoO_x standards and the absorption edge energy calculated using the formalism for direct-allowed electronic transitions ($\eta = {}^1/_2$). Detailed analysis, however, suggests that the fundamental absorption edge for crystalline MoO_3 arises from indirect-allowed electron transitions,[38] although analysis based on direct transitions leads to similar qualitative trends with domain size. This analysis based solely on the number of next nearest neighbors provides a useful directional relationship, but it neglects smaller shifts in the absorption edge energy as a result of differences in bonding configuration (edge- or corner-shared polyhedra) and of bonding between the polyhedra and the support. In this manner, the number of nearest neighbors in amorphous samples may be approximated using the absorption edge energy of crystalline standards if the details in bonding between polyhedra and support effects are also considered.

The absorption edge energy has also been shown to depend on crystallite size for small semiconductor nanocrystals (<100 nm) for which bonding geometry remains the same.[39] The energy of an electronic transition is well defined for any crystallite size. The momentum of the excited electron, however, becomes less accurately defined as the position is restricted by placing it within smaller crystallites. As a result, the separation among energy levels or bands increases as the crystallite size is reduced, as in the "particle-in-a-box" construct of elementary quantum mechanics. These quantum confinement effects have been described accurately by an analytical expression (eq 5) that can be used to calculate experimental shifts of absorption energies (ΔE) with crystallite size for crystallites larger than 2 nm.[19]

$$\Delta E = \frac{\hbar^2\pi^2}{2R^2}\left[\frac{1}{m_e} + \frac{1}{m_h}\right] - \frac{1.8e^2}{\epsilon R} + \text{polarization term} \quad (5)$$

This expression becomes inaccurate for domains smaller than 2 nm, because the periodic lattice and effective mass approximations required in its derivation become inappropriate. For these small domains (<2 nm), extended Hückel calculations have been used to predict the separation between energy levels.[40,41] Calculations for MoO_x clusters have confirmed that the separation between energy levels continues to increase for crystalline domains smaller than 2 nm.[41] These calculations have also confirmed that the HOMO−LUMO gap strongly depends on the number of nearest polyhedral neighbors and the number of bonds between each of those neighbors (corner- or edge-shared polyhedra).[41] In addition, these studies have shown that absorption energies are influenced less by the local symmetry around Mo^{6+} centers (tetrahedral or octahedral) and by the metal−oxygen bond lengths.

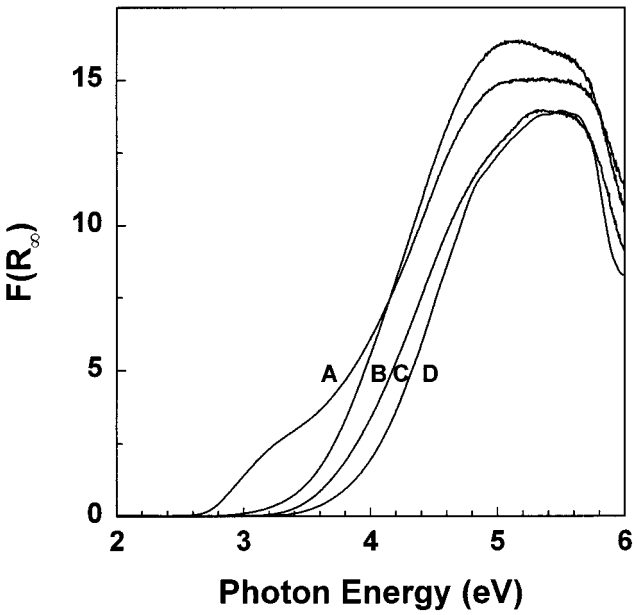

Figure 3. Diffuse reflectance UV−vis absorption spectra of a 26% WO_x−ZrO_2 sample oxidized at (A) 1073 K, (B) 973 K, (C) 873 K, and (D) 773 K.

3.3 UV−Visible Absorption Spectra of WO_x−ZrO_2 Samples. UV−vis diffuse reflectance absorption spectra of WO_x−ZrO_2 with varying WO_x concentrations and oxidation temperatures are shown in Figures 3−5. A sharp rise in absorption occurs between 2.6 and 3.6 eV as a result of ligand-to-metal charge transfer ($O_{2p} \rightarrow W_{5d}$−$O_{2p}$); the energy required for this transition depends strongly on WO_x concentration and oxidation temperature. UV−vis absorption spectra for a 26% WO_x−ZrO_2 sample oxidized at temperatures between 773 and 1073 K are shown in Figure 3. The absorption spectra shift to lower energies with increasing oxidation temperature and a second edge appears, at an energy similar to that in bulk monoclinic WO_3 crystals, when oxidation is carried out above 1073 K. On the latter samples, the presence of crystalline WO_3 has been confirmed by X-ray diffraction.[17] Increasing oxidation temperature leads to increased ZrO_2 sintering rates and loss of support surface area.[4] As a result, the average distance between dispersed WO_x octahedra on the ZrO_2 surface decreases and WO_x surface density increases with increasing oxidation temperature. As the coverage of the ZrO_2 support by WO_x species increases, the dispersed WO_x species eventually form W−O−W bridging bonds between neighboring WO_x groups, resulting in the formation two-dimensional polytungstates and three-dimensional WO_3 crystallites. The formation of these W−O−W bonds between WO_x octahedra leads to larger domains and to a narrowing of the HOMO−LUMO gap, as predicted by Masure et al.[41] and confirmed by the data in Figure 3.

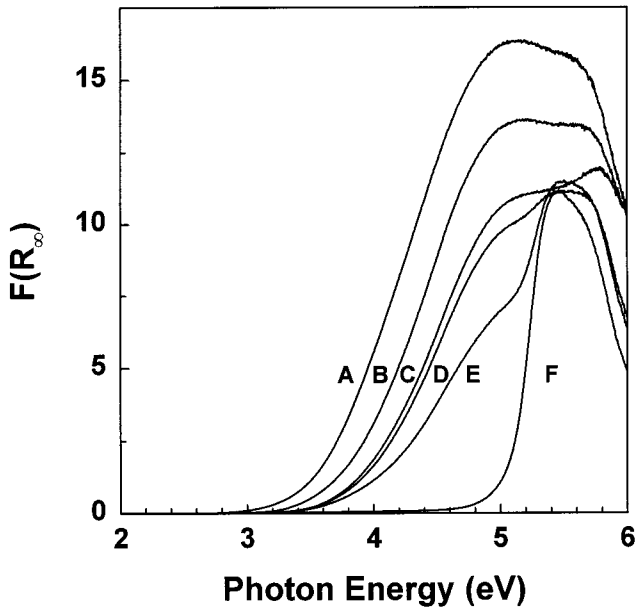

Figure 4. Diffuse reflectance UV−vis absorption spectra of WO_x−ZrO_2 samples oxidized at 973 K containing (A) 26%, (B) 20%, (C) 12%, (D) 9%, (E) 3%, and (F) 0% WO_3.

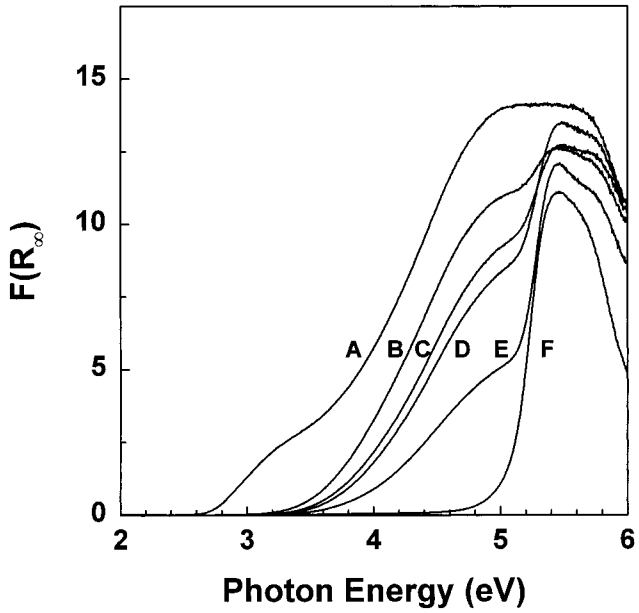

Figure 5. Diffuse reflectance UV−vis absorption spectra of WO_x−ZrO_2 samples oxidized at 1073 K containing (A) 26%, (B) 15%, (C) 12%, (D) 9%, (E) 3%, and (F) 0% WO_3.

Absorption spectra for several WO_x−ZrO_2 samples containing 3−26 wt % WO_3 oxidized at 973 K or at 1073 K are compared in Figures 4 and 5 with spectra for ZrO_2 (oxidized at 873 K). The absorption spectra for various crystalline ZrO_2 samples (not shown) are nearly independent of crystallite size and type (monoclinic or tetragonal); therefore, only a single ZrO_2 spectrum is included as reference. Clearly, a second absorption edge corresponding to ZrO_2 appears in all WO_x−ZrO_2 samples with WO_x concentrations less than 20 % WO_3. The intensity of the WO_x absorption edge increases and shifts to lower energies with increasing WO_x concentration as expected from the growth of WO_x domains by formation of corner- and edge-shared WO_x octahedra at higher WO_x surface densities. This increase in WO_x concentration has an effect similar to that of increasing the oxidation temperature, because they both tend to increase the WO_x surface density and domain size.

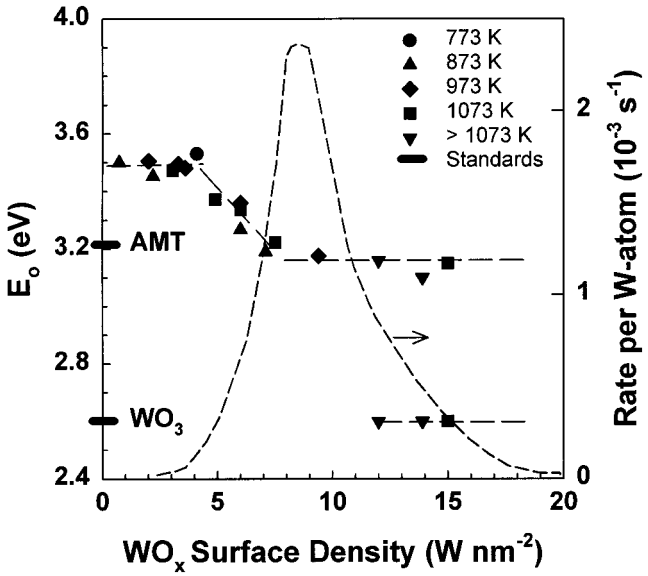

Figure 6. Indirect absorption edge energies of WO_x−ZrO_2 samples at several oxidation temperatures and tungsten loadings. Two crystalline tungsten oxide materials (monoclinic WO_3 and ammonium metatungstate) are shown for reference. Dashed curve is a summary of *o*-xylene isomerization rates per W atom,[15] [523 K, 0.66 kPa *o*-xylene, 100 kPa H_2].

3.4 UV−Visible Optical Absorption Edge Energies. *3.4.1 WO_x Surface Density and Domain Size.* Optical absorption edge energies were calculated from UV−vis diffuse reflectance spectra for the WO_x−ZrO_2 samples from Figures 3−5 and several other WO_x−ZrO_2 samples at other WO_x concentrations and oxidation temperatures using the formalism for indirect transitions given by eq 3 ($\eta = 2$). Absorption edge energies fall into a single curve for all samples when plotted against WO_x surface density (W nm^{-2}, from BET surface area measurements and WO_x concentration), irrespective of whether WO_x surface density changed because of varying WO_x concentration or oxidation temperature (Figure 6). Therefore, the electronic structure and the domain size of WO_x species on ZrO_2 surfaces depend only on WO_x surface density. In a previous study, we have also shown that the rate of *o*-xylene isomerization (per W atom) on these samples also depends only on WO_x surface density, and not the method used to achieve it.[15] The dashed "volcano curve" in Figure 6 shows the previously reported dependence of isomerization rate on WO_x surface density for comparison.

The data in Figure 6 suggest that absorption edge energies can be grouped into three distinct regions with characteristic surface density ranges of 0−4 W nm^{-2}, 4−8 W nm^{-2}, and >8 W nm^{-2}. Within the first region, the absorption edge energy is 3.49 ± 0.02 eV and it is not affected by WO_x surface density. In the second region, the absorption edge shifts linearly from 3.49 to 3.16 eV, and it maintains a constant value of 3.16 ± 0.05 eV above 8 W nm^{-2} in the third region. In this latter region, a second absorption edge appears at 2.6 eV, the absorption intensity of which increases monotonically with increasing WO_x surface density.

The density of acid sites (per W atom) detected by acid-catalyzed isomerization reactions reaches a maximum (reflected in the isomerization rate per W atom) at WO_x densities of about 8−9 W nm^{-2} (dashed curve in Figure 6). The data in this volcano-shaped curve also contain three distinct regions that can be grouped within ranges of WO_x surface densities (0−4, 4−9, and >9 W nm^{-2}) similar to those used for UV−visible edge energies. At low WO_x surface densities (<4 W nm^{-2}),

SCHEME 1. Evolution of Octahedral WO_x Species on ZrO_2 Surfaces with Increasing WO_x Surface Density

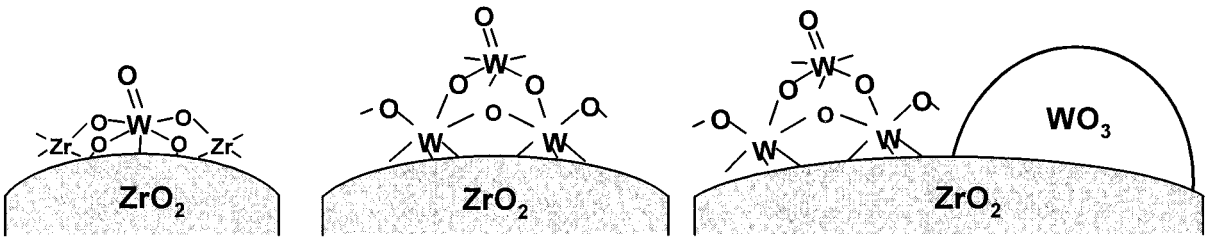

1a: (0-4 W nm^{-2}) 1b: (4-8 W nm^{-2}) 1c: (>8 W nm^{-2})

reaction rates are too low to measure. Isomerization rates increase with increasing WO_x density for values between 4 and 9 W nm^{-2}, and then decrease for densities higher than 9 W nm^{-2}. Near-edge X-ray absorption spectra of dehydrated WO_x-ZrO_2 with a wide range of WO_x surface density (3−15 W nm^{-2}) has shown that W^{6+} centers are present in distorted octahedra similar to each other and similar to those in crystalline WO_3 throughout the entire range of WO_x surface density. Thus, the observed changes in *o*-xylene isomerization rates cannot be attributed to the evolution of less-active tetrahedral WO_x into more active W species with octahedral structure as WO_x surface density increases, a process detected for WO_x species on $WO_x-Al_2O_3$ samples.[42] At low WO_x surface densities, tetrahedral WO_x species form on Al_2O_3 because stable $Al_2(WO_4)_3$-like species can form, whereas there are no tetrahedral WO_x species found on ZrO_2, because none of the known $Zr(WO_4)_2$ structures exhibit tetrahedral WO_x centers.

3.4.2 Low WO_x Surface Densities. WO_x-ZrO_2 samples with low WO_x surface densities (0−4 W nm^{-2}) show a constant absorption edge energy (3.49 eV) and contain very few acid sites capable of *o*-xylene isomerization at 523 K. The constant absorption edge energy suggests that the connectivity between WO_x groups is not influenced by surface density at low, submonlayer coverages. Extended Hückel calculations predict that the formation of metal oxide dimers and oligomers from isolated oxide species would shift absorption edge energies to lower values.[41] Apparently, WO_x groups do not interact with each other to form bridging W−O−W bonds until surface densities are greater than 4 W nm^{-2}. Below 4 W nm^{-2}, the ZrO_2 surface stabilizes dispersed WO_x species that are electronically isolated from each other (Scheme 1a). Near-edge X-ray absorption spectra show that these isolated WO_x species exist in distorted octahedral symmetry, and temperature-programmed reduction studies indicate that these species reduce in H_2 at significantly higher temperatures than polytungstate species or WO_3 crystallites.[4] The absorption edge energy for these dispersed WO_6 octahedra on ZrO_2 (3.49 eV) is significantly lower than the edge energy for truly isolated WO_4 tetrahedra in Na_2WO_4 (4.89 eV), and resemble more closely the dispersed WO_4 tetrahedra present on Al_2O_3 (3.95 eV). It is likely that the large distortions to the WO_x polyhedra caused by covalent bonds with ZrO_2 or Al_2O_3 increase the effective domain size of the dispersed WO_x polyhedra by allowing the delocalization of electrons within the Zr or Al next nearest neighbors, but to a lesser extent than when the next nearest neighbor is W.

Carbon dioxide chemisorption uptakes were used to measure the fraction of the ZrO_2 support covered by WO_x species. Carbon dioxide selectively binds to basic sites on ZrO_2 and therefore was used to determine the fraction of exposed ZrO_2. This method has been shown to accurately determine the coverage of TiO_2 supports by WO_x species.[43] The average value of CO_2 chemisorption uptakes at 313 K on several pure ZrO_2 samples oxidized at various temperatures (773−1073 K, 2.17 CO_2-molecules nm^{-2}) was used to determine the fraction of the ZrO_2 surface covered by WO_x. Carbon dioxide chemisorption uptakes on bulk WO_3 crystallites were negligible (0.01 CO_2-molecules nm^{-2}). The calculated WO_x coverage on ZrO_2 increases linearly as WO_x surface density increases within the submonolayer region (0−4 W nm^{-2}). WO_x coverages reach a constant value of about 90% at 4.0 W nm^{-2} and do not increase further as WO_x surface density increases, suggesting that a small fraction of basic sites on ZrO_2 remains exposed even at WO_x densities for which the condensation of WO_6 octahedra and formation of three-dimensional clusters occurs.

The linear increase in coverage with increasing WO_x surface density between 0 and 4 W nm^{-2} is consistent with well-dispersed WO_x species (Scheme 1a) that titrate CO_2 binding sites on ZrO_2 with 1:1 stoichiometry. Apparently, these isolated WO_x species are stabilized through multiple W−O−Zr bonds between each WO_6 octahedra and the ZrO_2 surface. These isolated WO_x octahedra reach saturation coverage (4 W nm^{-2}) at about half of the theoretical polytungstate monolayer (7.8 W nm^{-2}), which was estimated by the density of WO_x species in a two-dimensional plane of corner-shared WO_6 octahedra with W−O bond distances corresponding to those in low-index planes of monoclinic WO_3 crystallites. This saturation coverage of isolated monotungstate species on ZrO_2 agrees well with previous estimates from Raman spectroscopic data (4.0 W nm^{-2}).[22] At WO_x surface densities within the submonolayer region (0−4 W nm^{-2}), optical absorption spectra, CO_2 chemisorption uptakes, and X-ray absorption spectra are all consistent with the existence of isolated monotungstate WO_6 octahedra that are difficult to reduce and are not able to promote the isomerization of *o*-xylene at 523 K.

3.4.3 Intermediate WO_x Surface Densities. At intermediate WO_x surface densities (4−8 W nm^{-2}), absorption edge energies decrease and *o*-xylene isomerization rates per W atom increase markedly as WO_x surface density increases. The decrease in edge energy shows that electrons become delocalized in larger domains through bridging W−O−W bonds that are found within polytungstate two-dimensional structures (Scheme 1b) and small $(WO_3)_n$ clusters. Initial W−O−W bonds form by condensation of isolated WO_x species as the surface area of the ZrO_2 support decreases and the WO_x surface density increases during oxidation treatments. Increasing the surface density of WO_x species within this region (4−8 W nm^{-2}) leads to a monotonic increase in WO_x domain size until a constant domain size is reached corresponding to a polytungstate monolayer at about 8 W nm^{-2}. The density of WO_x species within this polytungstate monolayer is very similar to the theoretical polytungstate monolayer (7.8 W nm^{-2}).

The edge energies of these two-dimensional polytungstate structures (3.16−3.49 eV) are very similar to those in isopolytungstates (e.g., ammonium metatungstate, $(NH_4)_6H_2W_{12}O_{40}$, 3.25 eV) (Figure 6). Temperature-programmed reduction studies of WO_x-ZrO_2 samples with intermediate WO_x surface densities

SCHEME 2. Generation of Brønsted Acid Sites in the Presence of H_2 by Slight Reduction of a Neutral Polytungstate Structure and Charge Delocalization to Stabilize $H^{+\delta}$

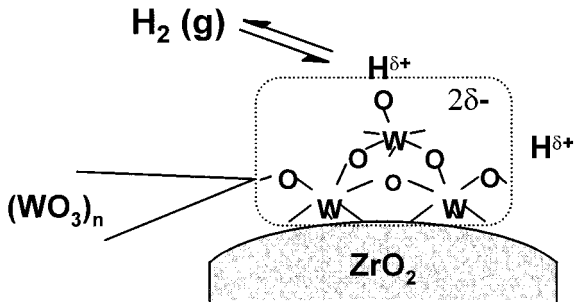

show that these polytungstate species begin to reduce at temperatures that are quite similar to a heteropolytungstate (12-tungstophosphoric acid) and at significantly lower temperatures than isolated WO_x species.[17] WO_x octahedra in these three-dimensional heteropolytungstates are connected within the wrapped surface and not through the center insulating atom; therefore, their domain size and reducibility is close to that of a two-dimensional polytungstate. Maximum *o*-xylene isomerization rates and therefore highest acid site densities are also found on WO_x-ZrO_2 catalysts near polytungstate saturation coverages because of an apparent compromise between WO_x accessibility to reactants and the ease of reduction of WO_x domains; the latter appears to be required in order to form Brønsted acid sites from neutral WO_x species[17] (Scheme 2). Hydrogen chemisorption and reduction measurements confirming this proposal are reported as a function of WO_x surface density in the last section of this paper. These measurements provide strong evidence for Brønsted acid site generation via the mechanism in Scheme 2.

3.4.4 High WO_x Surface Densities. At high WO_x surface densities (>8 W nm^{-2}), absorption edge energies remain constant at 3.19 eV and a second absorption edge appears at lower energies (2.61 eV) for surface densities above 12 W nm^{-2} (Figure 6). The intensity of this new absorption feature increases with increasing WO_x surface density and occurs at an energy similar to that in monoclinic WO_3 crystallites. X-ray diffraction detects the incipient formation of WO_3 crystallites at surface densities above 10 W nm^{-2}.[4] WO_3 crystallites on the latter WO_x-ZrO_2 samples are also apparent from their yellow color, their Raman spectra (Figure 8), and from the appearance of a distinct $WO_{2.9}$ to WO_2 reduction feature in temperature-programmed reduction profiles.[17] We have previously suggested that the decrease in *o*-xylene isomerization rates per W atom observed in these samples with increasing surface density is caused, in part, by a decrease in WO_x dispersion, which leads to inaccessible WO_x species within WO_3 crystallites.[17]

The absorption edge energy for polytungstate structures in samples containing WO_3-like absorption features is difficult to extract from experimental spectra because of significant overlap between WO_3 and polytungstate features. For these samples, a scaled spectrum for bulk WO_3 was subtracted from WO_x-ZrO_2 spectra in order to resolve the polytungstate absorption edge. Nonlinearities in the Kubelka−Munk function at high absorber concentrations resulted in imperfect fits when these pseudo-absorption spectra were used to describe the spectra for physical mixtures of pure crystalline WO_3 and ZrO_2. The absolute error in edge energies for these mixtures, however, was only ± 0.1 eV, and the method was used to obtain the edge energy values for samples with surface densities above 12 W nm^{-2} (Figure

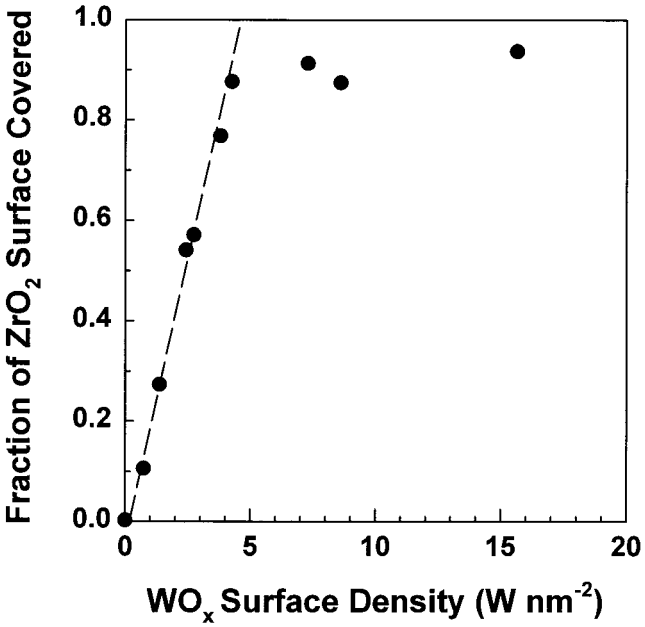

Figure 7. Fraction of ZrO_2 surface covered by WO_x species, determined by CO_2 chemisorption at 313 K.

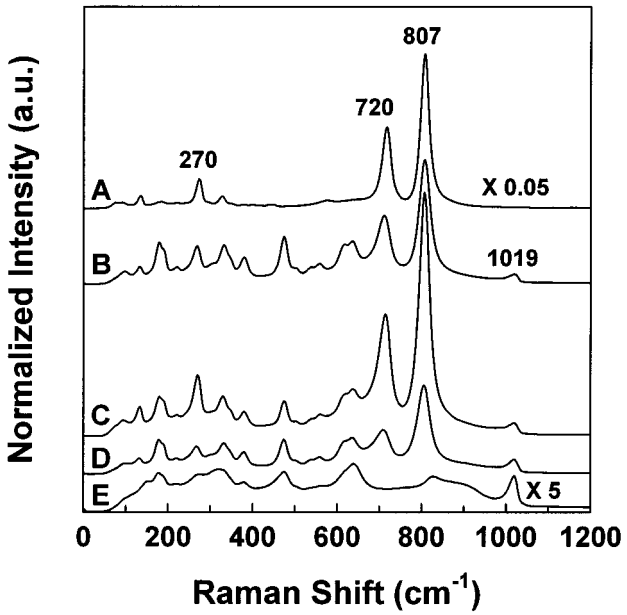

Figure 8. Raman spectra of (A) monoclinic WO_3, (B) 6% WO_x-ZrO_2 oxidized at 1223 K (11.2 W nm^{-2}), and 15% WO_x-ZrO_2 samples oxidized at (C) 1223 K (13.9 W nm^{-2}), (D) 1123 K (10.8 W nm^{-2}), and (E) 1023 K (4.5 W nm^{-2}).

6). These extracted edge energies are very similar to those measured for polytungstate species that lead to maximum *o*-xylene isomerization rates. This bimodal distribution of edge energies suggests that polytungstate monolayers on ZrO_2 are very stable and that WO_x species in excess of those required to form this monolayer bind weakly to it and tend to agglomerate into WO_3 crystallites during oxidation [Scheme 1c]. The stability of polytungstate monolayers on ZrO_2 is related to the strong W−O−Zr bonds between the WO_x octahedra and the ZrO_2 surface as suggested by high reduction temperatures of isolated WO_x species and by their stabilization of ZrO_2 surface area.[4] Crystallites of bulk WO_3 grow from the excess WO_x species because the W−O−W bonds that bind these octahedra to the polytungstate layer are weaker than the W−O−Zr bonds, and

at the high oxidation temperatures used these octahedra can migrate on the surface and agglomerate into crystals of WO_3 that minimize surface free energy.

An attempt to quantify the amount of crystalline WO_3 in WO_x-ZrO_2 samples based on the WO_3 absorption spectrum scaling factor gave inaccurate results. Samples containing similar amounts of bulk WO_3 but with different crystallite sizes resulted in a WO_3 scaling factor that varied with crystallite size. The penetration depth of photons in WO_x species is expected to be quite small at energies above the absorption edge energy; therefore, only a small fraction of the WO_x absorbers in a large WO_3 crystallite are probed by incoming photons. As a result, large WO_3 crystallites that consist primarily of internal WO_x species have a much smaller effective absorption cross sections than smaller WO_3 crystallites, making calculations of the amount of crystalline WO_3 from UV−vis absorption measurements inaccurate.

3.5 Raman Spectra of WO_x-ZrO_2 Samples. Raman spectra of several dehydrated WO_x-ZrO_2 samples and of crystalline WO_3 are shown in Figure 8. Polytungstate structures, with a Raman band at 880 cm^{-1},[22] are observed in the WO_x-ZrO_2 sample with the lowest WO_x surface density (4.5 W nm^{-2}, Figure 8(E)). The strong Raman feature at 1019 cm^{-1} in this sample has been assigned to the symmetric stretch mode of terminal W═O bonds,[44] which are present in monotungstate and polytungstate species and at the surface of WO_3 crystals. WO_x species also show Raman bands below 680 cm^{-1}, but these features overlap with those of tetragonal and monoclinic ZrO_2. The incipient formation of crystalline WO_3 appears at WO_x surface densities above 4.5 W nm^{-2}. Raman bands corresponding to crystalline WO_3 (Figure 8(A)) appear at 808, 720, and 275 cm^{-1}; these bands correspond to W−O stretching, W−O bending, and W−O−W deformation modes, respectively.[45,46] Raman scattering cross sections for crystalline WO_3 are much greater than for surface polytungstate species;[47] as a result, WO_3 bands tend to dominate the spectra and prevent the detection of polytungstate species, even when the latter are the most abundant surface structures. At intermediate WO_x surface densities (5−9 W nm^{-2}), the small WO_3 crystals detected by Raman are below the detection limit of X-ray diffraction and UV−vis absorption measurements. Their detection in Raman spectra suggest that the same mechanism that leads to polytungstate species occasionally leads to a very small fraction of weakly bound WO_x species that agglomerate into small WO_3 crystals. As WO_x surface density increases further, the bands at 807, 720, and 270 cm^{-1} become more intense, while the intensity of the 1019 cm^{-1} band remains almost constant.

In spectrum B (Figure 8(B); 6% WO_3, 1223 K oxidation, 11.2 W nm^{-2}), W−O bands for WO_3 clusters (270, 720, and 807 cm^{-1}) and terminal W═O bands (1019 cm^{-1}) are similar in intensity to those of samples with similar surface density (spectrum D; (15% WO_3, 1123 K oxidation, 10.8 W nm^{-2}) but with different WO_x concentration and oxidation temperature. These data confirm that WO_x structures depend only on WO_x surface density and not on WO_x concentration or oxidation temperature independently, a conclusion reached from the UV−vis data in the previous section.

The ratio of integrated peak areas of the W−O stretch (807 cm^{-1}) in microcrystalline WO_3 and the symmetric stretch of terminal (surface) W═O (1019 cm^{-1}) is shown in Figure 9 for dehydrated WO_x-ZrO_2 samples with various WO_x surface densities (3−28 W nm^{-2}). The intensity ratio increases from a value of zero for monotungstate species lacking W−O−W bonds (<5 W nm^{-2}) to very large values as the spectrum of large WO_3 crystallites becomes dominated by bulk W−O−W features. As WO_x surface density increases, the relative number of W−O bonds within microcrystalline WO_3 and polytungstate structures increases as WO_3 domains grow in size, while the number of surface (terminal) W═O remains almost constant. The observed increase in the ratio of intensities for these two bands shows that the concentration of WO_x species in WO_3 clusters increases as WO_x density increases. This is consistent with the UV−vis absorption edge results at >8 W nm^{-2}, which suggest that upon formation of a stable polytungstate monolayer on ZrO_2 excess weakly bound WO_x species readily agglomerate into WO_3 crystallites. The accessibility of WO_x species to reactants and their catalytic effectiveness decrease as WO_3 clusters grow with increasing surface density.

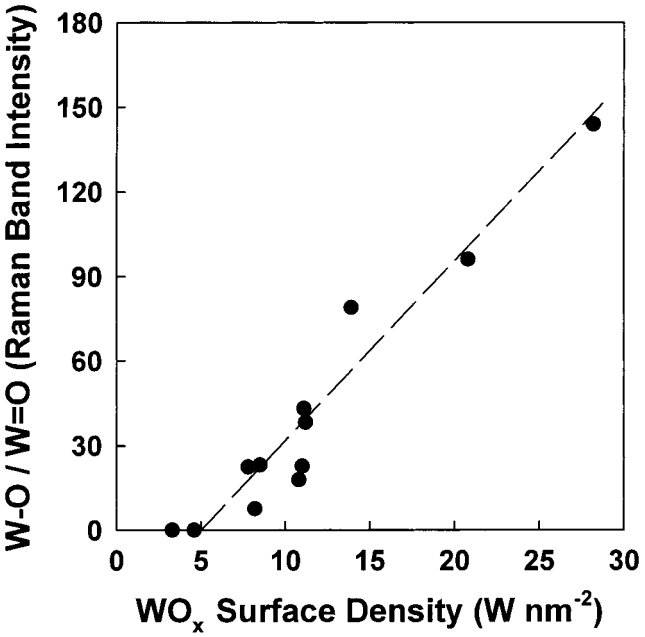

Figure 9. Relative increase in internal W−O bonds (807 cm^{-1}) with respect to terminal W═O bonds (1019 cm^{-1}).

3.6 Reduction of WO_x Species and the Formation of Brønsted Acid Sites and Color Centers in H_2. We have shown that *o*-xylene isomerization rates and acid site densities for WO_x species on ZrO_2 supports reach a maximum value at intermediate WO_x surface densities, for which a large fraction of the WO_x species reside on the surface of polytungstate clusters and Brønsted acid sites form by delocalization of an electron from an H atom resulting in $H^{+\delta}$ species.[15] H_2 has a promoting effect on the rate of acid catalysis on WO_x-ZrO_2, and appears to be required for the formation on Brønsted acid sites in neutral WO_x structures.[15]

WO_x-ZrO_2 samples with >4 W nm^{-2} acquire absorption bands in the visible region of the spectra in the presence of H_2 at a typical reaction temperatures (523 K). The appearance of absorption bands in the visible region can be visually detected by a change in color from white or light yellow to blue. In a similar manner, crystalline WO_3, yellow in color, forms a blue hydrogen bronze (H_xWO_3) in the presence of H_2 at 523 K, Figure 10. These color centers form in WO_x-ZrO_2 samples without any changes in the absorption edge energy, suggesting that their formation does not reflect changes in WO_x domain size, but instead changes caused by placement of H atoms at the surface and in the bulk of WO_x domains. Absorption of visible light at energies lower than the absorption edge occurs because electrons from the H atoms are inserted into the WO_3

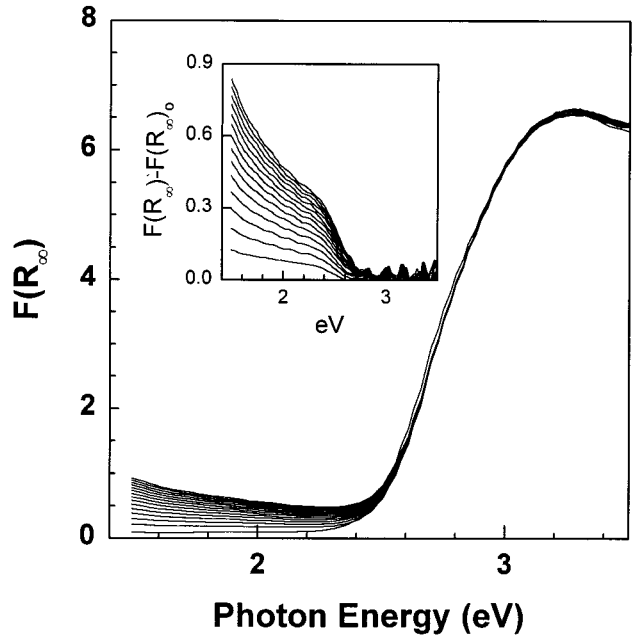

Figure 10. Reduction of monoclinic WO_3 in 100 kPa H_2 at 523 K with 0.5 h interval between scans. The inset shows the initial spectrum, $F(R_\infty)_o$, subtracted from each sample spectrum.

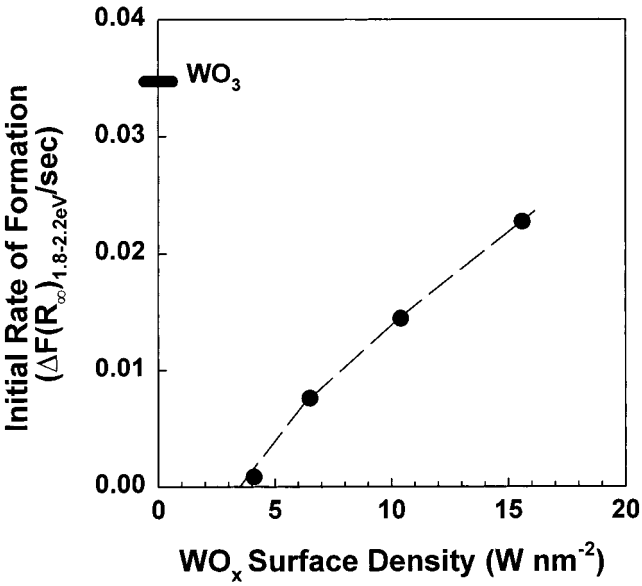

Figure 11. Initial rate of formation of tungsten oxide color centers in hydrogen at 523 K for a 26% WO_x-ZrO_2 sample oxidized at 773, 873, 973, and 1073 K, determined by integration of $F(R_\infty)$ from 1.8 to 2.2 eV. Initial rate of formation of color centers for bulk WO_3 plotted for reference.

LUMO and can be optically excited into unoccupied states available at slightly higher energies.[48] Similar processes appear to account for the appearance of Brønsted acidity; they require the presence of H_2 at temperatures sufficient for its dissociation and WO_x structures capable of stabilizing the resulting H atoms as $H^{+\delta}$ by the mechanism in Scheme 2.

The rate of formation of these color centers, which is related to the relative ability of the WO_x clusters to accommodate an H atom with its corresponding electron, was measured for several WO_x-ZrO_2 samples (26 wt % WO_3, 773−1073 K oxidation) with a wide range of WO_x surface densities (4−16 W nm^{-2}), Figure 11. Initial rates of formation were determined by integration of the Kubelka−Munk function ($(F(R_\infty))$ across

TABLE 1: Reversible H_2 Uptakes at 523 K and 27 KPa H_2 on WO_x-ZrO_2 Samples (26% WO_3, 773−1073 K Oxidation) after Reduction in H_2 at 523 K for 1 h

WO_x surface density (W nm^{-2})	reversible H_2 uptake (H atom/W atom)
4.1	0.001
6.5	0.009
8.5	0.026
15.6	0.010

the broad absorption band that appears during exposure to H_2 at 523 K in the visible region (1.8−2.2 eV). The rate of formation of color centers is very low for the WO_x-ZrO_2 sample with the lowest WO_x surface density (4.1 W nm^{-2}). These rates increase with increasing WO_x surface density, and they approach those measured on bulk WO_3 crystallites. This suggests that dispersed WO_x species cannot accommodate the negative charge required to stabilize $H^{+\delta}$, whereas polytungstate and crystalline WO_3 structures stabilize $H^{+\delta}$ with greater ease as WO_x domain size increases. The H atoms are stabilized by donation of an electron to electronegative WO_x domains (polytungstate or WO_3 clusters), which delocalize the negative charge with increasing effectiveness as the size of these WO_x domains increases. Apparently, as absorption edge energies decrease, WO_x domains accept electrons with greater ease because electrons are placed in unoccupied molecular orbitals available at lower energies. Effective WO_x-ZrO_2 solid acids require that WO_x domains must be large enough to stabilize negative charge and charge-compensating $H^{+\delta}$ species, but small enough to ensure that a large fraction of the $WO_x/H^{+\delta}$ remains accessible to reactants.

Hydrogen chemisorption uptakes were measured for several of these samples in order to determine the number of H atoms that reversibly bind to the WO_x species at typical *o*-xylene isomerization reaction temperatures (523 K) after hydrogen pretreatment and evacuation at the same temperature, Table 1. Maximum hydrogen uptakes were recorded on the WO_x-ZrO_2 sample showing maximum isomerization rates (0.026 H/W, 8.5 W nm^{-2}), suggesting that the formation of these reduced centers is indeed related to the stabilization of carbocationic intermediates. When the *o*-xylene isomerization rate on this WO_x-ZrO_2 sample is normalized to the hydrogen uptake the apparent Brønsted acid site turnover rate (8.1×10^{-2} (H atom)$^{-1}$ s^{-1}) is much higher than that reported for zeolites (H−ZSM5, Si/Al = 14.5, 0.17×10^{-2} (Al atom)$^{-1}$ s^{-1}) under similar reaction conditions (0.66 kPa *o*-xylene, 100 kPa H_2, 523 K).[49]

Hydrogen uptakes were very low on WO_x-ZrO_2 samples with low WO_x surface densities (0.001 H/W, 4.1 W nm^{-2}), because the isolated WO_x species are unable to delocalize the negative charge required to stabilize high $H^{+\delta}$ concentrations. Extended WO_x domains that form at higher WO_x surface densities can delocalize the negative charge throughout several WO_x neighbors. This mechanism of delocalization of charge among several WO_x groups and formation of Brønsted acid centers is similar to the generation of the strong acid sites on heteropolytungstate clusters, where the negative charge on the central anion is delocalized over the WO_x shell and balanced by H atoms with a net positive charge (e.g., 12-tungstophosphoric acid).[50] A much smaller hydrogen uptake was recorded in samples that contain large WO_3 crystallites (0.010 H/W, 15.6 W nm^{-2}) and show the highest rate of formation of color centers. The formation of color centers in WO_3 crystallites is known to occur by both the accommodation of H atoms in the lattice and by the thermal desorption of oxygen which leaves behind a more closely packed structure ($WO_{2.9}$) that has a reduced charge and is therefore unable to accommodate the additional charge to make $H^{+\delta}$. As

a result, the sharp decrease in catalytic activity at high WO_x surface densities may reflect the inability of large $WO_{2.9}$ domains to stabilize the additional electron required to accommodate H atoms as $H^{+\delta}$, as well as a decrease in accessibility of the WO_x species inside crystallites.

4. Conclusions

The domain size and structure of WO_x species on ZrO_2 supports were determined for a wide range of WO_x surface densities using UV−vis diffuse reflectance and Raman spectroscopies and CO_2 chemisorption. The WO_x domain size is controlled only by WO_x surface density and it is not influenced independently by WO_x concentration, oxidation temperature, and ZrO_2 surface area. Three distinct regions of WO_x coverage on ZrO_2 supports appear with increasing WO_x surface density: a submonolayer region (0−4 W nm^{-2}), a polytungstate growth region (4−8 W nm^{-2}), and a polytungstate/crystalline WO_3 coexistence region (>8 W nm^{-2}). At low WO_x surface densities, WO_x species strongly interact with ZrO_2 and they remain isolated; as a result, they are difficult to reduce and contain few acid sites that can isomerize *o*-xylene at 523 K. At intermediate WO_x surface densities, polytungstate domains grow with increasing WO_x surface density, WO_x species become easier to reduce, and *o*-xylene isomerization rates increase. At high WO_x surface densities, *o*-xylene isomerization rates decrease because a significant fraction of the WO_x species are found in the bulk of monoclinic WO_3 crystallites and are inaccessible to reactants.

The increase in *o*-xylene isomerization rates coincides with the growth of polytungstate species and a decrease in UV−vis absorption edge energy. This decrease in absorption edge energy reflects the condensation of WO_x octahedra and the growth of WO_x domains. Strong acid sites form on WO_x−ZrO_2 by the slight reduction of these polytungstate domains in the presence of H_2 at reaction temperatures (523 K). These $H^{\delta+}$ sites (Brønsted acid) sites form on larger WO_x domains because the electron from the H-atom may be delocalized throughout several neighboring octahedra.

WO_x−ZrO_2 samples containing crystalline WO_3 domains are less active per W atom because a fraction of the H atoms are accommodated inside the WO_3 crystals where they are inaccessible to hydrocarbon reactant molecules. In addition, crystalline WO_3 domains may reduce by loss of oxygen from the lattice, which would decrease the ability of these material to accept additional electrons from H atoms and form Brønsted acid sites.

Acknowledgment. The authors acknowledge financial support for this work from the National Science Foundation (CTS-9510575). The authors also thank Prof. Gustavo A. Fuentes of Universidad Autonoma Metropolitina-Iztapalapa, Mexico, for introducing us to UV−vis spectroscopy and for useful discussions.

Nomenclature

α = absorption coefficient
e = electron charge (C)
E_0 = optical absorption edge energy (eV)
ΔE = shift in edge energy (eV)
ϵ = dielectric constant
$F(R_\infty)$ = Kubelka-Munk function
h = Plank's constant
$\hbar = h/2\pi$
k = Boltzman's constant
m_e = effective mass of electron (kg)
m_h = effective mass of hole (kg)
η = electron transition exponent
ν = wavenumber (cm^{-1})
P_I = transition probability
R = radius of crystallite (m)
R_∞ = reflectivity ratio
R_i = reflectivity
S = scattering coefficient
σ = correlation parameter
T = temperature (K)

References and Notes

(1) Misono, M.; Okuhara, T. *Chemtech* **1993**, *23* (11), 23.
(2) Thomas, J. M. *Sci. Am.* **1992**, *266* 4, 112.
(3) Tanabe, K. *Solid Acids and Bases*; Academic Press: New York, 1970.
(4) Iglesia, E.; Barton, D. G.; Soled, S. L.; Miseo, S.; Baumgartner, J. E.; Gates, W. E.; Fuentes, G. A.; Meitzner, G. D. *Stud. Surf. Sci. Catal.* **1996**, *101*, 533.
(5) Arata, K. *Adv. Catal.* **1990**, *17*, 165.
(6) Tanabe, K.; Hattori, H.; Yamaguchi, T. *Crit. Rev. Surf. Chem.* **1990**, *1*, 1.
(7) Srinivasan, R.; Keogh, R. A.; Milburn, D. R.; Davis, B. H. *J. Catal.* **1995**, *153*, 123.
(8) Hino, M.; Arata, K. *J. Chem. Soc., Chem. Commun.* **1988**, 1259.
(9) Arata, K.; Hino, M. Proceedings of the 9th International Congress on Catalysis Calgary Alberta, 1988, p 1727.
(10) Soled, S. L.; Miseo, S.; Baumgartner, J. E.; Gates, W. E.; Barton, D. G.; Iglesia, E. Proceedings of the 13th International Conference on Catalysis, Kobe, Japan, 1994, p 17.
(11) Larsen, G.; Petkovic, L. M. *J. Mol. Catal. A−Chem.* **1996**, *113*, 517.
(12) Vaudagna, S. R.; Canavese, S. A.; Comelli, R. A.; Figoli, N. S. *Appl. Catal., A−Gen.* **1998**, *168*, 93.
(13) Hino, M.; Arata, K. *Appl. Catal., A−Gen.* **1998**, *169*, 151.
(14) Mobil Oil Corp., U.S. Patents 5, 345, 026, 1994; 5, 382, 731, 1995; 5, 401, 478, 1995; 5, 449, 847, 1995, 5, 453, 556, 1995; 5, 510, 309, 1996; 5, 516, 954, 1996; 5, 543, 036, 1996; 5, 552, 128, 1996; 5, 563, 310, 1996; 5, 563, 111, 1996; 5, 608, 133, 1997.
(15) Barton, D. G.; Soled, S. L.; Iglesia, E. *Top. Catal.* **1998**, *6*, 87.
(16) Pratt, K. C.; Sanders, J. V.; Christov, V. *J. Catal.* **1990**, *124*, 416.
(17) Barton, D. G.; Soled, S. L.; Meitzner, G. M.; Iglesia, E. *J. Catal.*, in press.
(18) Weber, R. S. *J. Catal.* **1995**, *151*, 470.
(19) Brus, L. E. *J. Chem. Phys.* **1984**, *80*, 4403.
(20) Wachs, I. E. *Catal. Today* **1996**, *27*, 437.
(21) Chan, S. S.; Wachs, I. E.; Murrell, L. L.; Dispenziere, N. C. J. *J. Catal.* **1985**, *92*, 1.
(22) Kim, D. S.; Ostromecki, M.; Wachs, I. E. *J. Mol. Catal., A−Chem.* **1996**, *106*, 93.
(23) Zhao, B.; Xu, X.; Gao, J.; Fu, Q.; Tang, Y. *J. Raman Spectrosc.* **1996**, *27*, 549.
(24) Gazzoli, D.; Valigi, M.; Dragone, R.; Marucci, A.; Mattei, G. *J. Phys. Chem.* **1997**, *101*, 11129.
(25) Kubelka, P.; Munk, F. *Z. Tech. Phys.* **1931**, *12*, 593.
(26) Smith, R. A. *Semiconductors*, 2nd ed.; Cambridge University Press: Cambridge, 1978.
(27) Tauc, J. In *Amorphous and Liquid Semiconductors*; Tauc, J., Ed.; Plenum: London, 1974; pp 159−220.
(28) Koffyberg, F. P.; Dwight, K.; Wold, A. *Solid State Commun.* **1979**, *30*, 433.
(29) Deb, S. K. *Philos. Mag.* **1973**, *27*, 801.
(30) Urbach, F. *Phys. Rev.* **1953**, *92*, 1324.
(31) Granqvist, C. G. *Handbook of Inorganic Electrochromic Materials*; Elsevier: Amsterdam, 1995.
(32) Stone, V. F.; Davis, R. J. *Chem. Mater.* **1998**, *10*, 1468.
(33) Iannibello, A.; Marengo, S.; Tittarelli, P. *J. Chem. Soc., Faraday Trans. 1* **1984**, *80*, 2209.
(34) Fournier, M.; Louis, C.; Che, M.; Chaquin, P.; Masure, P. *J. Catal.* **1989**, *119*, 400.
(35) Kortum, G. F. *Reflectance Spectroscopy*; Springer: New York, 1969.
(36) Okada, K.; Morikawa, H.; Marumo, F.; Iwai, S. *Acta Crystallogr. B* **1974**, *30*, 1872.
(37) Loopstra, O.; Boldrini, P. *Acta Crystallogr.* **1966**, *21*, 158.
(38) Carcia, P. F.; McCarron, E. M. *Thin Solid Films* **1987**, *155*, 53.
(39) Alivisatos, A. P. *Science* **1996**, *271*, 933.

(40) Jansen, S. A.; Singh, D. J.; Wang, S. H. *Chem. Mater.* **1994**, *6*, 146.

(41) Masure, D.; Chaquin, P.; Louis, C.; Che, M.; Fournier, M. *J. Catal.* **1989**, *119*, 415.

(42) Horsley, J. A.; Wachs, I. E.; Brown, J. M.; Via, G. H.; Hardcastle, F. D. *J. Phys. Chem.* **1987**, *91*, 4014.

(43) Vaidyanathan, N.; Houalla, M.; Hercules, D. M. *Catal. Lett.* **1997**, *43*, 209.

(44) Chan, S. S.; Wachs, I. E.; Murrell, L. L.; Wang, L.; Hall, W. K. *J. Phys. Chem.* **1984**, *88*, 5831.

(45) Ohwada, K. *Spectrochim. Acta A* **1970**, *26*, 1035.

(46) Anderson, A. *Spectrosc. Lett.* **1976**, *9*, 809.

(47) Chan, S. S.; Wachs, I. E.; Murrell, L. L. *J. Catal.* **1984**, *90*, 150.

(48) Gabrusenoks, J. V.; Cikmach, P. D.; Lusis, A. R.; Kleperis, J. J.; Ramans, G. M. *Solid State Ionics* **1984**, *14*, 25.

(49) Wilson, R. D.; Barton, D. G.; Iglesia, E. *J. Catal.*, submitted for publication.

(50) Pope, M. T. *Heteropoly and Isopoly Oxometalates*; Springer-Verlag: Berlin, 1983.